Predictions of NO and CO emissions in ammonia/methane/air combustion by LES using a non-adiabatic flamelet generated manifold

Takafumi Honzawa[*,a,b], Reo Kai[b], Akiko Okada[a], Agustin Valera-Medina[c], Philip J. Bowen[c], Ryoichi Kurose[b]

[a] *Fundamental Technology Department, Tokyo Gas Co., Ltd., 1-7-7 Suehiro-cho, Tsurumi-ku, Yokohama, Kanagawa 230-0045, Japan*

[b] *Department of Mechanical Engineering and Science, Kyoto University, Kyoto daigaku-Katsura, Nishikyo-ku, Kyoto 615-8540, Japan*

[c] *College of Physical Sciences and Engineering, Cardiff University, Queen's Building, Cardiff CF24 3AA, United Kingdom*

Abstract

A large-eddy simulation (LES) employing a non-adiabatic flamelet generated manifold approach, which can account for the effects of heat losses due to radiation and cold walls, is applied to NH_3/CH_4/air combustion fields generated by a swirl burner, and the formation mechanisms of NO and CO for ammonia combustion are investigated in detail. The amounts of NO and CO emissions for various equivalence ratios, are compared with those predicted by LES employing the conventional adiabatic flamelet generated manifold approach and measured in the bespoke experiments. The results show that the amounts of NO and CO emissions predicted by the large-eddy simulations with the non-adiabatic flamelet generated manifold approach agree well with the experiments much better than the ones with the adiabatic flamelet generated manifold approach. This is because the NO and CO reactions for NH_3/CH_4/air combustion are quite susceptible to H and OH radicals' concentrations and gas temperature. This suggests that it is essential to take into account the

*Corresponding Author. Tel.: +81-90-4021-9873; fax: +81-45-500-8790
Email address: honzawa.t@tokyo-gas.co.jp (Takafumi Honzawa)

effects of various heat losses caused by radiation and cold walls in predicting the NO and CO emissions for the combustion of ammonia as a primary fuel.

Key words: Non-adiabatic flamelet generated manifold approach, NH_3/CH_4/air combustion, Large-eddy simulation, Nitrogen oxides, Carbon monoxide

---

Highlights

- LES employing non-adiabatic flamelet approach is employed for NH_3/CH_4/air combustion.
- Heat losses affect NO and CO emissions, which can be captured by the simulation.
- NO and CO reactions are susceptible to H and OH concentrations and gas temperature.
- Temperature dependency of NO reaction is different between NH_3/CH_4/air and CH_4/air.

---

1. Introduction

The emissions of carbon dioxide (CO_2), which induces global warming, is increasing at a rapid rate. In Japan, 39% of CO_2 emissions are discharged in energy transformation industries such as power generation plants [1], and the most are produced by combustion of fossil fuels. The amount of the CO_2 emissions in gas power plants is approximately one half of that in coal-fueled power plants [2]. Therefore, while renewable energy plants such as solar and wind power plants increase, the demand of gas power plants is considered to remain in order to maintain the supply of electricity. But it is necessary to reduce the CO_2 emissions in gas power plants more than now.

Ammonia (NH_3) combustion has recently drawn intense research interest because of its potential to reduce CO_2 emissions when implemented in such power plants. NH_3 is

17.8% by weight hydrogen, a relatively high hydrogen ratio [3, 4]. The technologies related to its production, transportation, and storage are well established, with NH_3 being the second largest produced chemical in the world. NH_3 can be also produced from renewable energy sources [5]. In addition, NH_3 can be easily liquefied and stored in the conditions of 8.5 bar at ambient temperature or 240 K at ambient pressure, which is less expensive than liquefying pure hydrogen [6]. Therefore, NH_3 has been considered as a potential source of hydrogen and an alternative carbon-free fuel for the future. As the first step, it will be an actual solution to mix NH_3 and conventional fossil fuels in order to reduce CO_2 emissions.

Considerable research on NH_3 combustion has been done since the 1960s [7-9]. Experimental studies showed that the minimum ignition energy of NH_3 is 16 times higher than that of fossil fuels. At stoichiometric conditions, the quenching distance of NH_3/air was 3.5 times greater than that of propane/air [8]. Other experiments demonstrated that NH_3/air has a relatively slow chemical reaction rate, giving a laminar burning velocity of 6-8 cm/s [10], which is only one fifth that of methane (CH_4)/air. In other studies, high production of nitrogen oxides (NOx) originating from nitrogen in NH_3 is considered as a problem [11-13].

In the face of such problems for NH_3 combustion, some challenges for the practical application have been conducted recently. Valera-Medina et al. [14, 15] combusted NH_3/CH_4/air in various equivalence ratios in a laboratory-scale tangential swirl burner and suggested low swirl and different injection strategies to optimize gas turbines with NH_3 as a primary fuel. Kurata et al. [16] demonstrated NH_3/CH_4/air combustion employing a micro gas turbine in the Fukushima Research Energy Institute. Hayakawa et al. [17] showed that a specific equivalence ratio supports low emissions of nitric oxide (NO) and NH_3.

Because NOx emissions are strictly regulated, an optimized burner design for NH_3 combustion is required. For such purposes, computational fluid dynamics (CFD) can be an

effective approach. Somarathne et al. [18] illuminated the effect of secondary air injection to reduce the amount of NO emissions. It was suggested that the equivalence ratio, ϕ, at the primary zone should be controlled as $\phi = 1.2$. This indicates that the equivalence ratio in an ideal combustion chamber changes from a fuel-rich condition to a stoichiometric condition. Additionally, the NO production rate is relatively slow and depends on temperature. Therefore, to evaluate the amount of NO emissions, it is necessary to consider heat losses in combustion chambers. However, the simulations in previous researches were conducted in an adiabatic condition using detailed reaction mechanisms [18, 19]. There is no study that examined the validity of turbulence combustion models, especially flamelet approaches.

The purpose of this study is, therefore, to perform large-eddy simulation (LES) using two types of flamelet approach for NH_3/CH_4/air combustion in the swirl burner [15], and to validate our method by comparing the amounts of NO and carbon monoxide (CO) emissions with experimental data. At the beginning, in order to investigate an adequate mechanism for the condition of the swirl burner, some representative detailed reaction mechanisms are compared through evaluating the laminar burning velocity and the amount of NO emissions. Then, LESs with two types of flamelet approach are conducted. As a combustion model, a non-adiabatic flamelet generated manifold approach (NA-FGM), which is extended based on the conventional flamelet-generated manifold approach (FGM) [20]. The NA-FGM can consider the effects of various heat losses through radiation and cold walls. Proch and Kempf [21] employed the NA-FGM for a tabulated premixed flame. In their approach, progress variable, progress variable variance and enthalpy difference were introduced for generating the flamelet library, whereas mixture fraction is additionally introduced in this study, in order to take into account the variation of ϕ. In addition, the NO and CO reactions are discussed in non-adiabatic conditions from the viewpoint of chemical

reactions.

2. Numerical methods

2.1. Configurations of targeted chamber and swirl burner

Figure 1 shows schematics of computational domain and generic swirl burner. The detailed structure of this burner is identified in the previous studies [15, 22]. The fuel consists of 61.0% NH_3 and 39.0% CH_4 by volume, and the oxidizer is air. This fuel component gave stable NH_3-based flames in the experiments, and NO and CO emissions were measured [15]. The NH_3/CH_4/air premixed gas is supplied from the inlet nozzle. Its equivalence ratio is set as 0.840, 1.04 and 1.31 respectively. Because the gas is completely mixed in advance, the variance of the composition is ignored. Progress variables C of any inlet gases are zero. Here, C is defined as the sum of Y_{H2}, Y_{H2O}, Y_{CO} and Y_{CO2}. Y_i denotes the mass fraction of chemical species i. After passing through the swirler, the premixed gas is burned in the combustion chamber made of a quartz glass. The domain is divided into ~5 million vertices and ~6 million cells. The small meshes are provided to resolve the turbulent eddies in the recirculating reaction zones.

As boundary conditions, the volume flow rate of fuel at the inlet is constant as 1.35 x 10^{-3} m^3/s. The inlet premixed gas temperature is 298 K, and the ambient pressure is 1 atm. If the LES/NA-FGM is employed, temperature, convection heat transfer rate, and emissivity on the walls of the combustion chamber are set to 1500 K, 10 W/m^2K, and 0.8 respectively. The other walls are treated adiabatically. Since these properties on the walls could not be measured in the experiment, these parameters on the boundary conditions are based on our experiences. On the other hand, the all walls are treated adiabatically if the conventional LES/FGM is employed.

Here, the swirl number, Sw, of the burner is also addressed. Sw can be defined as

$$Sw = \frac{G_a}{G_r r_1}, \quad (1)$$

where G_a and G_r are respectively the angular and radial momenta, and r_1 is the radius of the tubular cavity of the swirler. Velocity at the slit, w_s, is expressed as $w_s = Q/(n_s t_s L_s)$, where Q is total volume flow rate, and n_s, t_s and L_s are respectively the number of slits, the thickness and the longitudinal length for each slit. The angular momentum per unit volume for the premixed gas is $\rho w_s(r_1 - t_s/2)$. Here, $(r_1 - t_s/2)$ is the distance between the axis and the center of the slits. Because of the above, the total angular momentum, G_a, is expressed as $G_a = \rho Q w_s(r_1 - t_s/2) = \rho Q^2(r_1 - t_s/2)/(n_s t_s L_s)$. On the other hand, mean axial velocity, U, is expressed as $U = Q/(\pi r_1^2)$. Accordingly, the total radial momentum, G_r, is expressed as $G_r = \rho Q U = \rho Q^2/(\pi r_1^2)$. Therefore, Sw is expressed as

$$Sw = \frac{1}{\pi}\frac{\left(r_1 - \frac{t_s}{2}\right) r_1}{n_s t_s L_s}. \quad (2)$$

In this study, because r_1 = 20 mm, n_s = 9, t_s = 5.7 mm and L_s = 18.5 mm, Sw is 1.84.

2.2. LES/NA-FGM

For numerical simulations of premixed combustion, premixed flamelet libraries based on the FGM [20], for which one-dimensional premixed free-propagating flame is calculated in several equivalence ratios, are often used. However, the conventional FGM has the deficiency that a set of chemical species' mass fractions at the equilibrium state of the reaction is basically stored in adiabatic conditions, so that the effect of heat loss on the change in the composition of chemical species cannot be considered. In this study, therefore, a non-adiabatic procedure, which was proposed by Kishimoto et al. [23] for generating non-premixed flamelet libraries that consider the effects of heat losses based on the flamelet/progress-variable approach [24], is employed for generating the premixed flamelet

library. The calculations of the one-dimensional free-propagating flames for generating the premixed flamelet libraries for the FGM and NA-FGM are conducted by using FlameMaster [25], for which the non-adiabatic procedure [23] is introduced.

The results of one-dimensional premixed flames calculated in physical space is converted to low dimensional manifold parameterized by mixture fraction Z, progress variable C, and enthalpy difference Δh, shown as

$$\varphi = \varphi(Z, C, \Delta h), \tag{3}$$

where φ is flamelet properties such as temperature, chemical species mass fraction and so on. Δh is the difference between the absolute enthalpy without heat loss in the flamelet library and that with heat loss in the physical space at each vertex. In LES, the Favre-filtered flamelet library can be obtained as

$$\tilde{\varphi}\left(\tilde{Z}, \widetilde{C''^2}, \tilde{C}, \widetilde{\Delta h}\right) = \int_0^1 \varphi(Z, C, \Delta h) P(C) dC, \tag{4}$$

where $P(C)$ is the density weighted filter probability function of the progress variables, and beta sub-filter distribution of the progress variable is shown as

$$P\left(C; \tilde{C}, \widetilde{C''^2}\right) = \frac{C^{\beta_1 - 1}(1-C)^{\beta_2 - 1}}{\int_0^1 C^{\beta_1 - 1}(1-C)^{\beta_2 - 1} dC}. \tag{5}$$

Here, β_1 and β_2 are given as

$$\beta_1 = \beta_1\left(\tilde{C}, \widetilde{C''^2}\right) = \tilde{C}\left(\tilde{C}\frac{1-\tilde{C}}{\widetilde{C''^2}} - 1\right), \tag{6}$$

$$\beta_2 = \beta_2\left(\tilde{C}, \widetilde{C''^2}\right) = \left(1 - \tilde{C}\right)\left(\tilde{C}\frac{1-\tilde{C}}{\widetilde{C''^2}} - 1\right), \tag{7}$$

where $\tilde{C}$ is grid scale and $\widetilde{C''^2}$ is sub-grid scale variable component.

The numbers of grids set for $\tilde{Z}$, $\tilde{C}$, $\widetilde{C''^2}$, and, $\Delta\tilde{h}$, are 100 × 100 × 50 × 4. The discrete points of $\tilde{C}$, $\widetilde{C''^2}$ and$\Delta\tilde{h}$ are arranged at regular intervals. Accordingly to Z, 98 points are regularly arranged among Z = 0.057 and Z = 0.12, and points of Z = 0.0 for only oxidizer and Z = 1.0 for only fuel are added.

The governing equations for the LES employing the FGM and NA-FGM are the same. They are the conservation equations of mass, momentum, absolute enthalpy $\tilde{h}$, mixture fraction $\tilde{Z}$, and progress variable $\tilde{C}$, and NO mass fraction $\widetilde{Y_{NO}}$ as follows:

$$\frac{\partial \bar{\rho}}{\partial t} + \nabla \cdot (\bar{\rho}\tilde{\boldsymbol{u}}) = 0. \tag{8}$$

$$\frac{\partial \bar{\rho}\tilde{\boldsymbol{u}}}{\partial t} + \nabla \cdot (\bar{\rho}\tilde{\boldsymbol{u}}\tilde{\boldsymbol{u}}) = -\nabla \bar{P} + \nabla \cdot \bar{\boldsymbol{\sigma}} + \nabla \cdot \tau. \tag{9}$$

$$\frac{\partial \bar{\rho}\tilde{h}}{\partial t} + \nabla \cdot \left(\bar{\rho}\tilde{\boldsymbol{u}}\tilde{h}\right) = \nabla \cdot \left(\bar{\rho}\widetilde{D_h}\nabla\tilde{h}\right) + \nabla \cdot \boldsymbol{q}_h + Q_{\text{rad}}. \tag{10}$$

$$\frac{\partial \bar{\rho}\tilde{Z}}{\partial t} + \nabla \cdot \left(\bar{\rho}\tilde{\boldsymbol{u}}\tilde{Z}\right) = \nabla \cdot \left(\bar{\rho}\widetilde{D_Z}\nabla\tilde{Z}\right) + \nabla \cdot \boldsymbol{q}_Z. \tag{11}$$

$$\frac{\partial \bar{\rho}\tilde{C}}{\partial t} + \nabla \cdot \left(\bar{\rho}\tilde{\boldsymbol{u}}\tilde{C}\right) = \nabla \cdot \left(\bar{\rho}\widetilde{D_C}\nabla\tilde{C}\right) + \nabla \cdot \boldsymbol{q}_C + \widetilde{\dot{\omega}_C}. \tag{12}$$

$$\frac{\partial \bar{\rho}\widetilde{Y_{NO}}}{\partial t} + \nabla \cdot \left(\bar{\rho}\tilde{\boldsymbol{u}}\widetilde{Y_{NO}}\right) = \nabla \cdot \left(\bar{\rho}\widetilde{D_{Y_{NO}}}\nabla\widetilde{Y_{NO}}\right) + \nabla \cdot \boldsymbol{q}_{Y_{NO}} + \bar{\rho}\widetilde{\dot{\omega}_{NO}}. \tag{13}$$

Here, $\boldsymbol{u}$ is the velocity, P is the pressure, $\boldsymbol{\sigma}$ is the stress tensor. D_h, D_Z, D_C and $D_{Y_{NO}}$ are the diffusion coefficients of h, Z, C and Y_{NO}, respectively, which are given as

$$D_\varphi = \frac{\mu}{Pr_\varphi}, \tag{14}$$

where μ is dynamic viscosity, and Pr_φ is Prandtl number of each transport scalar φ. Pr_φ = 0.7 are used for the simulations. τ is the subgrid-scale stress term derived from the turbulence model, and $\boldsymbol{q}_h$, $\boldsymbol{q}_Z$, $\boldsymbol{q}_C$ and $\boldsymbol{q}_{Y_{NO}}$ are the subgrid-scale terms for each scalar. Q_{rad} is the source term of radiative heat transfer. $\bar{\varphi}$ and $\tilde{\varphi}$ denote the LES filtering and Favre averaging of a physical quantity φ, respectively. $\dot{\omega}_C$ is the reaction rate of C. Temperature is calculated from transported enthalpy with the species mass fractions and these thermal data.

It is well-known that reactions related to NO are slow. NO concentration in the flamelet libraries is calculated at the equilibrium state. The reactions are often affected by heat losses in practical combustion chambers. In that case, the concentration is not

coincident with experimental results. Then, NO concentration is evaluated based on Ihme and Pitsch's approach [26]. They proposed the method that the forward and backward NO reaction rates are separately modeled with the reaction rates taken from the flamelet library as,

$$\widetilde{\dot{\omega}_{NO}} = \widetilde{\dot{\omega}_{NO}^{+}} + \tilde{Y}_{NO}\frac{\widetilde{\dot{\omega}_{NO}^{-}}}{\tilde{Y}_{NO}^{flm}}, \tag{15}$$

where $\widetilde{\dot{\omega}_{NO}^{+}}$ and $\widetilde{\dot{\omega}_{NO}^{-}}$ denote forward and backward reaction rate, respectively, and $\tilde{Y}_{NO}^{flm}$denotes NO mass fraction in the flamelet libraries. Therefore, for the LES/NA-FGM, the slow rate of the NO reactions in non-adiabatic conditions can be considered. On the other hand, for the LES/FGM, the rate in an adiabatic condition is considered.

2.3. Computational details

The governing equations are solved using an unstructured LES solver: FrontFlow/Red extended by some research institutes, including Kyoto University, referred to as FFR-Comb [23, 27, 28]. Previously, the NA-FPV was implemented to the LES solver and the accuracy of non-adiabatic procedure is validated [23]. In this study, the NA-FGM is newly implemented to the code.

A dynamic Smagorinsky model [29] is used as the turbulence model. A first-order Euler implicit method is used for time advancement, and the time step is set to 1.0 x 10^{-5} s. The flamelet libraries for the FGM and NA-FGM are built using the mechanisms developed by the University of California San Diego [30] with nitrogen chemistry [31] in this study. This mechanism has 70 species and 321 reaction steps. The reason for selecting this mechanism is expressed in section 3.1. A gray gas model is adopted as the radiation model [32]. The absorption constant is 0.10, which is determined by reference to the results of

RANS simulation with weighted sum of gray gasses model [33].

As ignition process, the initial value of the progress variable, C, is set to 0.5 at the region which is from 20 mm to 50 mm from the burner rim and within 15 mm from the center axis. After that, the calculations are continued until the fields reach steady state.

3. Results and discussion

3.1. Validation of reaction mechanism

The predicted combustion behavior is strongly affected by the detailed reaction mechanism used in the LES. Therefore, in this section, the effects of the detailed reaction mechanism on the laminar burning velocity, S_L, and NO emissions are investigated in terms of one- and two-dimensional simulations, respectively. As the detailed reaction mechanism, GRI-mech 3.0 [34], and the mechanisms developed by the University of California San Diego [30] with nitrogen chemistry [31], Tian et al. [35], and Okafor et al. [36] are featured. Here, these mechanisms are respectively referred to as GRI-mech, UCSD-mech, Tian-mech, and Okafor-mech which was developed by combining GRI-mech and Tian-mech.

3.1.1. Laminar burning velocity by one-dimensional simulations

One-dimensional adiabatic and unstretched laminar premixed flames of NH_3/CH_4/air mixtures are calculated using ANSYS Chemkin-PRO [37]. This application is used for comparing various reaction mechanisms, because the FlameMaster cannot deal with complex mechanisms such as Tian-mech and Okafor-mech. It is found the cause that these mechanisms have NH + NO = N_2O + H as an important elementary reaction and the pre-exponential factor is negative value. S_L is defined as the velocity at the cold boundary in the computational domain.

Figure 2 shows the comparison of S_L obtained by one-dimensional calculations

using different detailed reaction mechanisms, together with experiments of Okafor et al. [36]. The fuel consists of 52.1% NH_3 and 47.9% CH_4 by volume, and this constituent is close to that in the swirl burner. Tian-mech overestimates S_L in the whole ϕ range. Although GRI-mech shows good accuracy, the reactions related to NH_2, which is an important species for the NO reactions, are not included [38]. Okafor-mech shows a good agreement in a wide range of ϕ. Finally, although UCSD-mech matches the experimental results at $\phi > 1$, it somewhat overestimates at $\phi < 1$.

3.1.2. NO emissions by two-dimensional simulations

Two-dimensional RANS (Reynolds-Averaged Navier-Stokes) simulations are conducted in order to compare the amount of NO emissions using each reaction mechanism. There are no previous studies that evaluated the amount of NO emissions for NH_3/CH_4/air laminar flames, so the experiment conditions by Valera-Medina et al. [15] are taken up in order to qualitatively evaluate each reaction mechanism.

Figure 3 shows the schematic of computational domain for two-dimensional RANS simulations. The domain is divided into ~90 thousand cells. As the conditions regarding the composition of the premixed gases, its flow rate and temperature and pressure are the same in section 2.1. For the premixed gas, the uniform radial velocity, V, and uniform circumferential velocity, W, are used as the inlet boundary condition. V and W are respectively expressed as

$$V = \frac{Q}{2\pi r_1 L_s}, \tag{16}$$

$$W = \frac{Q}{n_s t_s L_s}. \tag{17}$$

Wall conditions are adiabatic and any radiation model is not employed, due to focus on the elementary adequateness of each reaction mechanism for the swirl burner. Realizable k-ε

model [39] is employed as a turbulence model.

Figure 4 shows the comparison of temperature distributions obtained by two-dimensional RANS simulations using different detailed reaction mechanisms at ϕ = 0.840, 1.04 and 1.31, respectively. The distributions by GRI-mech, UCSD-mech and Okafor-mech are quite similar at each ϕ condition. There is great difference for only Tian-mech. Although Tian-mech overestimates laminar burning velocity, the flame is lifted up from the bottom of the burner. In the experimental study, the actual flame was not lifted up at ϕ = 1.31 [15]. Therefore it is assumed thatTian-mech is incompatible with the conditions of this study.

Figure 5 shows the comparison of the amounts of NO emissions obtained by two-dimensional RANS simulations using different detailed reaction mechanisms, together with experiments [15]. The NO concentrations for the whole conditions by the simulations reach the steady state before approaching the outlet boundary. All mechanisms overestimate the amounts of NO emissions in the whole ϕ range in comparison with the experimental results. The amount of NO emissions using UCSD-mech is comparatively close to the experimental result except for Tian-mech. NO emissions with both of Okafor-mech and UCSD-mech are similar at ϕ = 0.840 and 1.04, but the amount of NO emissions at ϕ = 1.31 with Okafor-mech is 1.55 times larger than that with UCSD-mech.

As above, because UCSD-mech has a relatively reasonable agreement among these mechanisms and can be dealt by the FlameMaster, it is employed for generating the flamelet libraries and discussing the NO and CO reactions in non-adiabatic conditions.

3.2. Predictions of NO and CO emissions by LES

3.2.1. NO emissions

First, Fig. 6 shows the comparisons of distributions of (a) temperature, (b) axial

velocity, (c) OH mole fraction, and (d) NO mass fraction at $\phi = 1.31$ between the LES/FGM and the LES/NA-FGM. The maximum temperature for the LES/FGM is 1974 K, the same as the adiabatic flame temperature, T_{ad}. However, the LES/NA-FGM shows 1950 K, and it is lower than the T_{ad} by 24 K by heat losses. There are no differences in terms of flow field between these approaches. The difference in OH mole fraction distributions, which is one of the most important species for the NH_3 combustion, should be addressed. Once OH is produced in the LES/FGM, the concentration remains high throughout the combustion process. However, OH in the LES/NA-FGM is produced only in the flame region, and, after leaving this region, it disappears. This is the reason that the production of NO in the LES/NA-FGM is lower than that in the LES/FGM. The effects of temperature and the presence of H and OH radicals are discussed in section 3.3.1. Figure 7 shows the comparisons of axial profiles of NO concentration and temperature at $\phi = 1.31$ between the LES/FGM and the LES/NA-FGM. NO concentrations for both approaches rapidly decrease through passing each flame zone. After that, the NO concentration for the LES/FGM remains almost the same in the downstream. This is explained by Fig. 8, which shows the correlation between production rate of NO and progress variable, C, at $\phi = 0.840$, 1.04 and 1.31for $\Delta h = 0$ (FGM). The production rate of NO in the downstream of a flame is negative at only $\phi = 1.31$, and when the value of C becomes its maximum, the rate is almost zero. The LES/FGM estimates the amount of NO emissions as 148 ppm in Fig. 7. However, the NO concentration for the LES/NA-FGM monotonically decreases even in the downstream of a flame, and eventually reaches 9 ppm. This value is close to 7 ppm measured in the experiments [15]. This shows the superiority of the LES/NA-FGM in estimating the amount of NO emissions, and it also shows the quantitative accuracy at $\phi = 1.31$.

Second, Fig. 9 shows the comparisons of distributions of (a) temperature, (b) axial velocity, (c) OH mole fraction, and (d) NO mass fraction for the LES/NA-FGM between

the cases of $\phi = 0.840$ and 1.04. The maximum of OH mole fraction at $\phi = 0.840$ and 1.04 is larger by approximately 15 times than that at $\phi = 1.31$, increasing the reactivity at these ϕ conditions. As a result, the NO production is quite high, especially at $\phi = 0.840$. Each of NO concentrations at $\phi = 0.840$ and 1.04 for the LES/NA-FGM also decreases in the downstream of the flames. This is the peculiar behavior derived from the presence of heat losses, because the NO production rate in the downstream of a flame zones is almost zero in adiabatic conditions in Fig. 8.

Figure 10 shows the comparison of the amounts of NO emissions as a function of ϕ between the LES/FGM and the LES/NA-FGM, together with the results obtained by one-dimensional premixed flame calculations (PREMIX) and experiments [15]. For comparison, the NO concentrations at the outlet boundary for one-dimensional laminar premixed flames are also illustrated as PREMIX. The amount of NO emissions for the LES/FGM is proximate to that for the PREMIX and is higher than that of the experiment for whole ϕ conditions, whereas that for the LES/NA-FGM is estimated quantitatively at $\phi > 1.04$. However, it is overestimated by more than twice, at $\phi = 0.840$, even when the LES/NA-FGM is employed. The reasons of the overestimation are as follows. First, the experiment at $\phi = 0.840$ may include an uncertainty. According to the experiment, the amount of O_2 emissions at $\phi = 0.840$ is approximately 4.5%. The concentration corresponds to that as $\phi = 0.752$ if the premixed gas is completely burned. However, because the amount of NO emissions at $\phi = 0.752$ for the LES/NA-FGM is still high in Fig. 10, it cannot be concluded that the experimental condition was equivalent to not as $\phi = 0.840$ but as $\phi = 0.752$. Second, some inaccuracies remain in UCSD-mech employed in this study. UCSD-mech overestimates S_L at $\phi < 1$, and the reactions concerning NO are still not validated. At $\phi = 0.840$, there is very few effect on the consumption rate of NO in non-adiabatic conditions in section 3.3.1. If this should be the case, it means that

UCSD-mech overestimates the NO production in a flame zone. For the quantitative prediction of NO emissions at ϕ = 0.840, these unclear problems must be separately examined.

3.2.2. CO emissions

Because CO emissions are often problematic for practical uses because of its harmful effect on human bodies, this section deals with their evaluation. Figure 11 shows the comparisons of distributions of CO mole fraction at ϕ = 0.840, 1.04 and 1.31 between the LES/FGM and the LES/NA-FGM. Once CO in the LES/FGM is produced at ϕ = 1.04 and 1.31, the concentration remains high. This is the effect of thermal dissociation, and one part of CO_2 transforms into CO in high temperatures. This transformation is hardly seen in the LES/NA-FGM because of heat losses.

Finally, Fig. 12 shows the comparison of the amounts of CO emissions at ϕ = 0.840 between the LES/FGM and the LES/NA-FGM, together with the experiments [15]. The experimental results for other ϕ conditions were not accurately measured because of an upper limit of equipment range. At ϕ = 0.840, the amount of CO emissions in the LES/FGM is overestimated, whereas that in the LES/NA-FGM is close to the experimental result, which emphasizes that the LES/NA-FGM is a more accurate tool to determine the amount of CO emissions.

3.3. Effects of heat losses on NO and CO reactions

The effects of heat losses on the NO and CO reactions are investigated in detail in terms of one-dimensional premixed flame calculations below. The UCSD-mech is employed as the detailed reaction mechanism as ever. The fuel consists of 61.0% NH_3 and 39.0% CH_4 by volume, and the unburned temperature and pressure are 298 K and 1 atm,

respectively.

3.3.1. NO reactions

The reactions related to NO are slower than others. Therefore, it is assumed that heat losses affect the consumption rate of NO in the downstream region of flames. Figure 13 shows the time series of NO concentrations at ϕ = 0.840, 1.04 and 1.31 for NH_3/CH_4/air combustion obtained by one-dimensional calculations in non-adiabatic conditions. Here, the downstream region of a flame is defined as the downstream side from the position that H mole fraction reaches the maximum. The all species' concentrations at the time in an adiabatic condition are used as each initial condition. Then, the change of NO concentrations is calculated under constant temperature, T, in downstream regions. Besides, T_{ad} shows the adiabatic flame temperature at each ϕ condition.

At ϕ = 0.840, the NO concentrations are not changed other than the case of T = 1900 K, and it slightly decreases at T = 1900 K. At ϕ = 1.04, the NO concentration at T = T_{ad} remains over 4000 ppm. On the other hand, it dramatically decreases in non-adiabatic conditions, and especially at T = 2000 K, it eventually reaches 204 ppm. As temperature becomes lower than T = 2000 K, the consumption rate becomes slower, and the NO concentration at T = 1500 K rather increases and heads for 6300 ppm. That is, this value is larger than that in the adiabatic condition. Finally, at ϕ = 1.31, the NO concentrations become diminished as temperature decreases. In the case of T = 1900 K and 1800 K, the NO concentrations gradually decrease, and they eventually reach about 6 ppm. NO instantaneously disappears in the cases of T < 1700 K.

For comparison, Fig. 14 shows the time series of NO concentrations at ϕ = 0.840, 1.04 and 1.31 for CH_4/air combustion obtained by one-dimensional calculations in non-adiabatic conditions. At ϕ = 0.840 and 1.04, the production rate of NO increases

through thermal NO_X processes as temperature becomes higher. For CH_4/air combustion, there is no specific temperature condition which strengthens the consumption of NO, and this trend is different from NH_3/CH_4/air combustion. On the other hand, the NO concentration decreases slowly at $\phi = 1.31$, and the consumption rate of NO becomes max at around 1900 K.

For NH_3/CH_4/air combustion, Fig. 15 shows the relevant reaction path related to the NO concentration at $\phi = 1.31$ at the time that its consumption rate is max by one-dimensional calculation in a non-adiabatic condition. The ambient temperature is $T = 1900$ K. The thickness of each arrow denotes the relative magnitude of the reaction rate. NO is mainly consumed through three routes, or N_2O, N_2H and N_2 route respectively.

$$NO + NH = N_2O + N \quad (18)$$

$$NO + NH_2 = N_2H + OH \quad (19)$$

$$NO + N = N_2 + O \quad (20)$$

$$NO + NH = N_2 + OH \quad (21)$$

$$NO + NH_2 = N_2 + H_2O \quad (22)$$

In the N_2O route, N_2O changes to N_2 by reacting with H or OH radical. Moreover, NH_2 and NH, which are needed for above reactions, are generated from NH_3 and NH_2, respectively. These reactions require H and OH radicals. Therefore, it is important for the consumption of NO that there are active radicals such as O and OH in non-adiabatic conditions.

As above, the effects of heat losses on the consumption of NO are not almost observed at $\phi = 0.840$, but the NO concentration slightly decreases at only $T = 1900$ K. At $\phi = 1.04$, NO concentration decreases the fastest at $T = 2000$ K, and as temperature becomes smaller, it rather increases. At $\phi = 1.31$, NO concentrations at $T = 1900$ K and 1800 K decrease gradually to about 6 ppm, and in the cases of $T < 1700$ K, it instantaneously disappears. Such heat losses and active radicals such as H and OH support the consumption

of NO.

3.3.2. CO reactions

Figure 16 shows the principal reactions of CO at ϕ = 0.840 for NH_3/CH_4/air combustion obtained by one-dimensional calculation in an adiabatic condition. The consumption rate of CO basically depends on one reaction,

$$CO + OH = CO_2 + H. \quad (23)$$

OH radical is namely the most important species.

In order to evaluate the effects of heat losses, ambient temperature dependence for the consumption of CO is investigated. Figure 17 shows the time series of CO concentrations at ϕ = 0.840 for (a) NH_3/CH_4/air combustion and (b) CH_4/air combustion, which are obtained by one-dimensional calculations in non-adiabatic conditions. The definition of the downstream region is the same as the previous section. For NH_3/CH_4/air combustion, the consumption rate of CO becomes larger with rich OH radicals under low ambient temperature. As temperature becomes lower than T_{ad}, the consumption rate of CO becomes faster, and the rate becomes max around 1500 K. At T = 1500 K, the concentration reaches a few ppm within 40 ms. The consumption rate at T = 1200 K becomes slower than that at T = 1500 K, but the concentration reaches under 1 ppm after the passage of 200 ms. Because the required time is much larger than the reaction time of other main species, the transport equation of CO must be additionally employed in LES for the prediction of CO emissions in such non-adiabatic conditions. In other words, in this study, it is assumed that the amount of CO emissions can be evaluated without its transport equation. At T = 900 K, CO reactions are completely stopped and the concentration remains quite high. Additionally, the behavior of the CO concentration for CH_4/air combustion is almost the same as that for NH_3/CH_4/air combustion.

4. Conclusions

In this study, a large-eddy simulation (LES) employing a non-adiabatic flamelet generated manifold approach (NA-FGM), which can account for the effects of various heat losses caused by radiation and cold walls, was applied to NH_3/CH_4/air combustion fields generated by a swirl burner, and the formation mechanisms of NO and CO for ammonia combustion were investigated in detail. The amounts of NO and CO emissions for various equivalence ratios, ϕ, were compared with those predicted by LES employing the conventional adiabatic flamelet generated manifold approach (FGM) and measured in the bespoke experiments [15]. The results obtained in this study are summarized as follows.

(1) The amounts of NO and CO emissions predicted by the LES/NA-FGM agree well with the experiments much better than the LES/FGM. This is because the NO and CO reactions for NH_3/CH_4/air combustion are quite susceptible to H and OH radicals' concentrations and gas temperature. This suggests that it is essential to take into account the effects of various heat losses caused by radiation and cold walls in predicting the NO and CO emissions for the combustion of ammonia as a primary fuel.

(2) Regarding the NO emissions, the amount is successfully predicted using the LES/NA-FGM for $\phi > 1.04$, whereas it is overestimated at $\phi = 0.840$. This is considered to be due to the UCSD-mech used for generating the flamelet libraries. This mechanism tends to overestimate S_L, which may produce NO excessively in a flame zone.

Acknowledgments

The author would like to thank Mr. M. Seino and Mr. T. Nishiie of Numerical Flow Designing Co., Ltd. for their help for developing the simulation code. The author also thank

Prof. Kobayashi, Assistant Prof. Hayakawa and Dr. Okafor of Tohoku University for their advice for selecting reaction mechanisms. Cardiff University gratefully acknowledges the support from the Welsh European Funding Office (WEFO) project no. 80835.

References

[1] Y. Nojiri, S. Harasawa, E. Hatanaka, A. Hayashi, H. Ito, N. Kosaka, T. Oda, A. Osako, K. Sakai, M. Yanagawa, National Greenhouse Gas Inventory Report of JAPAN (2017), National Institute for Environmental Studies, Japan. ISSN: 1341-4356.

[2] V. Krey, O. Masera, G. Blanford, T. Bruckner, R. Cooke, K. Fisher-Vanden, H. Haberl, E. Hertwich, E. Kriegler, D. Mueller, S.Paltsev, L. Price, S. Schlömer, D. Ürge-Vorsatz, D. van Vuuren, T. Zwickel, IPCC Working Group III - Mitigation of Climate Change, Annex II: Metrics and Methodology (2014), available at http://pure.iiasa.ac.at/id/eprint/11109/.

[3] K. Goshome, T. Yamada, H. Miyaoka, T. Ichikawa, Y. Kojima, High compressed hydrogen production via direct electrolysis of liquid ammonia, Int. J. Hydrogen Energy 41 (2016) 14529-14534.

[4] C. Zamfrescu, I. Dincer, Ammonia as a green fuel and hydrogen source for vehicular applications, Fuel Process. Technol. 90 (2009) 729-737.

[5] R. Michalsky, B.J. Parman, V. Amanor-Boadu, P.H. Pfromm, Solar thermochemical production of ammonia from water, air and sunlight: Thermodynamic and economic analyses, Energy 42 (2012) 251-260.

[6] S.J. yang, H. Jung, T. Kim, C.R. Park, Recent advances in hydrogen storage technologies based on nanoporous carbon materials, Prog. Nat. Sci. 22 (2012) 631-638.

[7] F.J. Verkamp, M.C. Hardin, J.R. Williams, Ammonia combustion properties and performance in gas-turbine burners, Int. Symp. Combust. 11 (1) (1967) 985-992.

[8] D.T. Pratt, Performance of ammonia fired gas turbine combustors, Report TR-9-TS-67-5, Solar San Diego, USA (1967).

[9] H. Newhall, E. Starkman, Theoretical performance of ammonia as a gas turbine fuel, SAE tech. pap. 660768 (1966).

[10] J. Li, H. Huang, N. Kobayashi, Z. He, Y. Nagai, Study on using hydrogen and ammonia as fuels: Combustion characteristics and NOx formation, Int. J. Energy Research 38 (2014) 1214-1223.

[11] O. Mathieu, E.L. Petersen, Experimental and modeling study on the high-temperature oxidation of ammonia and related NOx chemistry, Combust. Flame 162 (2015) 554-570.

[12] K. Ryu, G.E. Zackarakis-Jutz, S.C. Kong, Performance enhancement of ammonia-fueled engine by using dissociation catalyst for hydrogen generation, Int. J. Hydrogen Energy 39 (2014) 2390-2398.

[13] W.E. Lear, Ammonia-Fueled Combustion Turbines, available at https://nh3fuel.files.wordpress.com/2012/05/lear_nh3.pdf.

[14] A. Valera-Medina, S. Morris, J. Runyon, D.G. Pugh, R. Marsh, P. Beasley, T. Hughes, Ammonia, methane and hydrogen for gas turbines, Energy Procedia 75 (2015) 118-123.

[15] A. Valera-Medina, R. Marsh, J. Runyon, D. Pugh, P. Beasley, T. Hughes, P. Bowen, Ammonia–methane combustion in tangential swirl burners for gas turbine power generation, Applied Energy 185 (2017) 1362-1371.

[16] O. Kurata, N. Iki, T. Matsunuma, T. Inoue, T. Tsujimura, H. Furutani, H. Kobayashi, A. Hayakawa, Performances and emission characteristics of NH_3-air and NH_3-CH_4-air combustion gas-turbine power generations, Proc. Combust. Inst. 36 (2017) 3351-3359.

[17] A. Hayakawa, Y. Arakawa, R. Mimoto, K.D.K.A. Somarathne, T. Kudo, H. Kobayashi, Experimental investigation of stabilization and emission characteristics of ammonia/air premixed flames in a swirl combustor, Int. J. Hydrogen Energy 42 (2017) 14010-14018.

[18] K.D.K.A. Somarathne, S. Hatakeyama, A. Hayakawa, H. Kobayashi, Numerical study

of a low emission gas turbine like combustor for turbulent ammonia/air premixed swirl flames with a secondary air injection at high pressure, Int. J. Hydrogen Energy 42 (2017) 27388-27399.

[19] H. Xiao, A. Valera-Medina, P. Bowen, S. Dooley, 3D simulation of ammonia combustion in a lean premixed swirl burner, Energy Procedia 142 (2017) 1294-1299.

[20] J.A. Van Oijen, L.P.H. De Goey, Modelling of premixed laminar flames using flamelet-generated manifolds, Combust. Sci. Tech. 161 (1) (2000) 113-137.

[21] F. Proch, A.M. Kempf, Modeling heat loss effects in the large eddy simulation of a model gas turbine combustor with premixed flamelet generated manifolds, Proc. Combust. Inst. 35 (3) (2015) 3337-3345.

[22] J. Runyon, R. Marsh, A. Valera-Medina, A. Giles, P. Bowen, Methane-oxygen flame stability in a generic premixed gas turbine swirl combustor at varying thermal power and pressure, ASME turbo expo. (2015) GT2015-43588.

[23] A. Kishimoto, H. Moriai, K. Takenaka, T. Nishiie, M. Adachi, A. Ogawara, R. Kurose, Application of a non-adiabatic flamelet/progress-variable approach to Large Eddy Simulation of H2/O2 combustion under a pressurized condition, J. Heat Transfer 139 (12) (2017) 124501.

[24] C.D. Pierce, P. Moin, Progress-variable approach for large-eddy simulation of non-premixed turbulent combustion, J. Fluid Mech. 504 (2004) 73-94.

[25] H. Pitsch, FlameMaster, A C++ Computer Program for 0D Combustion and 1D Laminar Flame Calculation (1998), https://web.stanford.edu/group/pitsch/FlameMaster.htm.

[26] M. Ihme, H. Pitsch, Modeling of radiation and nitric oxide formation in turbulent nonpremixed flames using a flamelet/progress variable formulation, Phys. Fluids 20 (2008) 055110.

[27] H. Moriai, R. Kurose, H. Watanabe, Y. Yano, F. Akamatsu, S. Komori, Large-eddy simulation of turbulent spray combustion in a subscale aircraft jet engine combustor-predictions of no and soot concentrations, J. Eng. Gas Turbines Power 135 (2013) 091503.

[28] S. Tachibana, K. Saito, T. Yamamoto, M. Makida, T. Kitano, R. Kurose, Experimental and numerical investigation of thermo-acoustic instability in a liquid-fuel aero-engine combustor at elevated pressure: Validity of large-eddy simulation of spray combustion, Combust. Flame 162 (2015) 2621-2637.

[29] M. Germano, U. Piomelli, P. Moin, W.H. Cabot, A dynamic subgrid‐scale eddy viscosity model, Phys. Fluids A 3 (1991) 1760-1765.

[30] Chemical Kinetic Mechanism for Combustion Applications, Center for Energy Research (Combustion Division), University of California at San Diego, available at http://web.eng.ucsd.edu/mae/groups/combustion/sdmech/sandiego20161214/sandiego20161214_mechCK.txt.

[31] Chemical Kinetic Mechanism for Combustion Applications, Center for Energy Research (Combustion Division), University of California at San Diego, available at http://web.eng.ucsd.edu/mae/groups/combustion/sdmech/sandiego_nitrogen/NOx_20041209/NOXsandiego20041209.mec.

[32] M.F. Modest, Radiative Heat Transfer, Academic Press, U.S. (2013).

[33] T.F. Smith, Z.F. Shen, J.N. Friedman, Evaluation of coefficients for the weighted sum of gray gases model, J. Heat Transfer 104 (1982) 602-608.

[34] G.P. Smith, D.M. Golden, M. Frenklach, N.W. Moriarty, B. Eiteneer, M. Goldenberg, et al., GRI-mech 3.0, Gas Research Institute, available at http://www.me.berkeley.edu/gri_mech/.

[35] Z. Tian, Y. Li, L. Zhang, P. Glaborg, F. Qi, An experimental and kinetic modeling study

of premixed $NH_3/CH_4/O_2/Ar$ flames at low pressure, Combust. Flame 156 (7) (2009) 1413-1426.

[36] E.C. Okafor, Y. Naito, S. Colson, A. Ichikawa, T. Kudo, A. Hayakawa, H. Kobayashi, Experimental and numerical study of the laminar burning velocity of CH_4-NH_3-air premixed flames, Combust. Flame 187 (2017) 185-198.

[37] CHEMKIN-PRO 18.2, ANSYS, Inc.: San Diego (2017).

[38] A. Hayakawa, T. Goto, R. Mimoto, Y. Arakawa, T. Kudo, H. Kobayashi, Laminar burning velocity and Markstein length of ammonia/air premixed flames at various pressures, Fuel 159 (2015) 98-106.

[39] T.H. Shih, W.W. Liou, A. Shabbir, Z. Yang, J. Zhu, A new k-ϵ eddy viscosity model for high reynolds number turbulent flows, Computers Fluids 24 (3) (1995) 227-238.

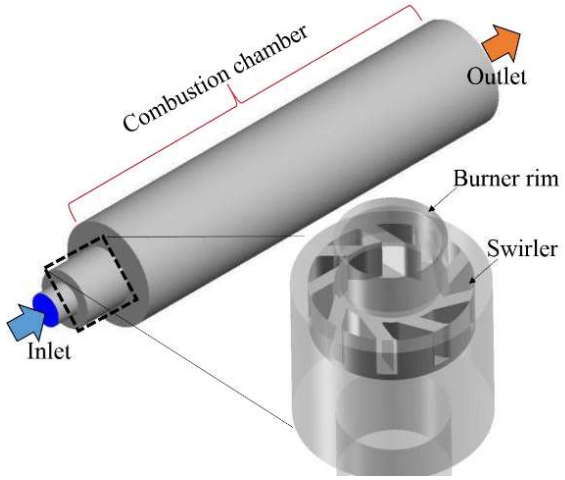

Fig. 1: Schematics of computational domain and generic swirl burner [15].

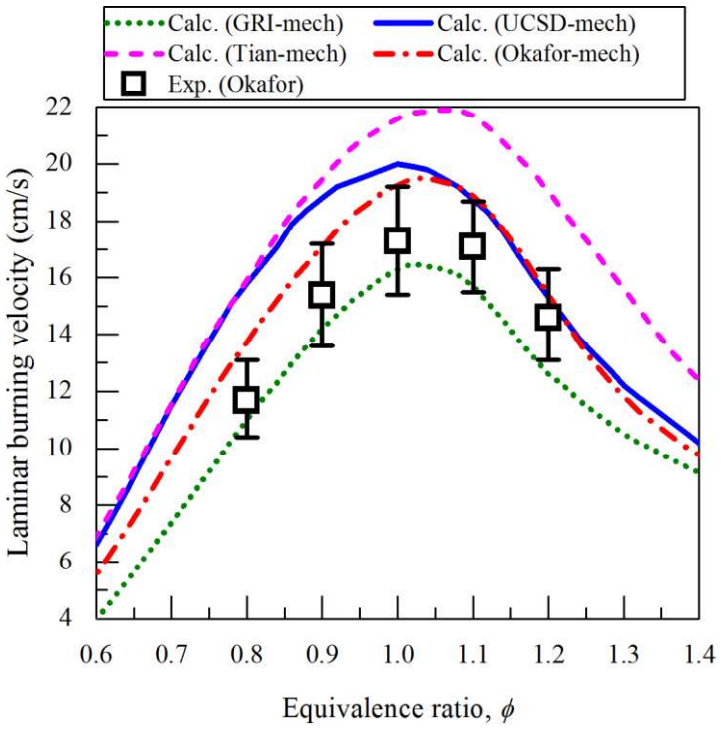

Fig. 2: Comparison of laminar burning velocities obtained by one-dimensional calculations using different detailed reaction mechanisms, together with experiments [36].

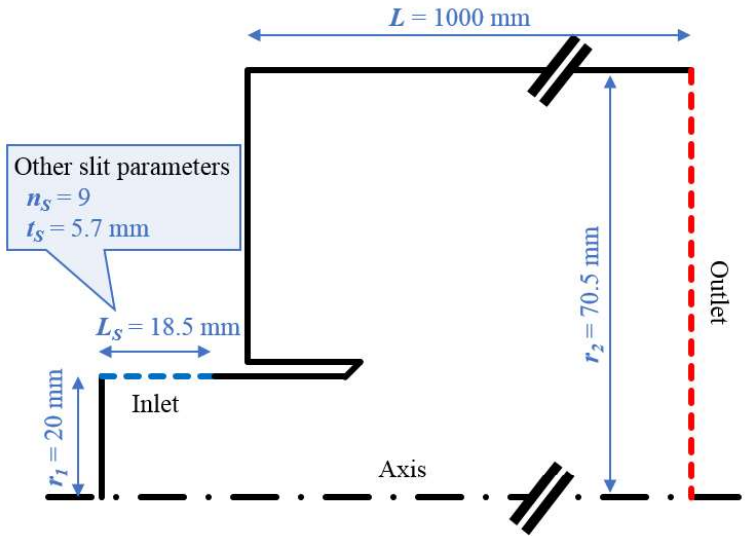

Fig. 3: Schematic of computational domain for two-dimensional RANS simulations.

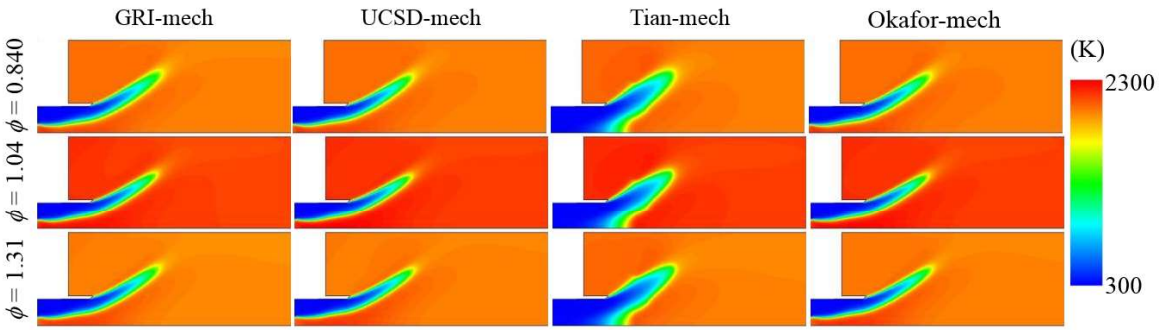

Fig. 4: Comparison of instantaneous temperature distributions obtained by two-dimensional RANS simulations using different detailed reaction mechanisms at ϕ = 0.840, 1.04 and 1.31.

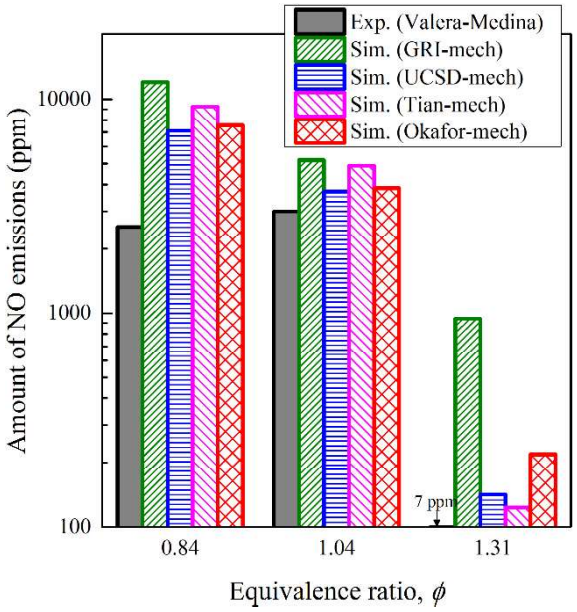

Fig. 5: Comparison of time-averaged amounts of NO emissions obtained by two-dimensional RANS simulations using different detailed reaction mechanisms, together with experiments [15].

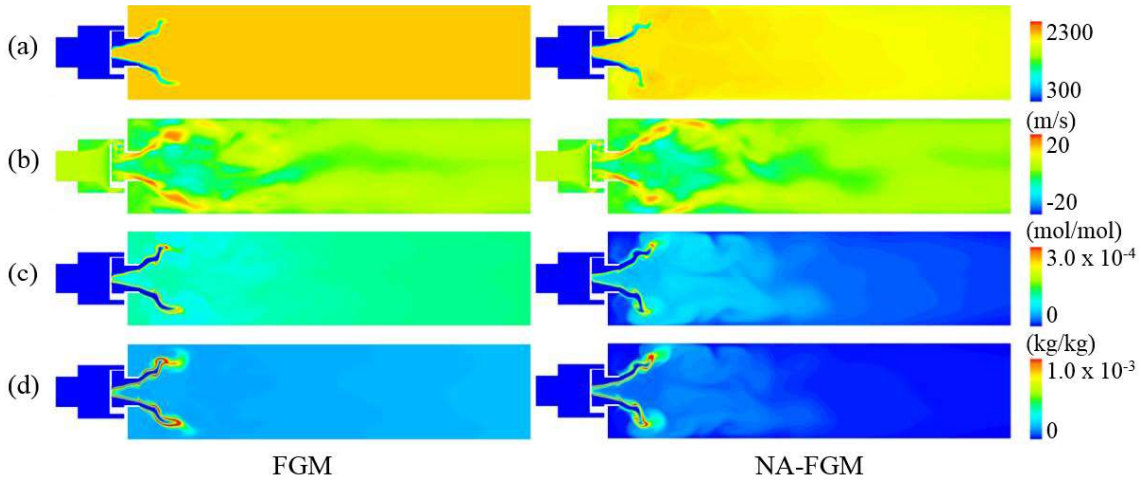

Fig. 6: Comparisons of instantaneous distributions of (a) temperature, (b) axial velocity, (c) OH mole fraction, and (d) NO mass fraction at ϕ = 1.31 between LES/FGM and LES/NA-FGM.

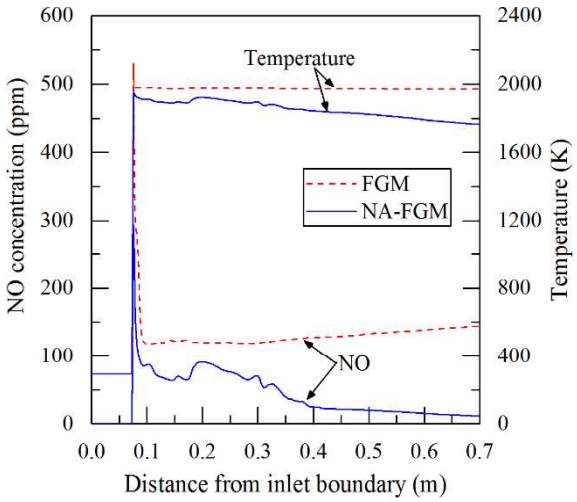

Fig. 7: Comparisons of time-averaged axial profiles of NO concentration and temperature at $\phi = 1.31$ between LES/FGM and LES/NA-FGM.

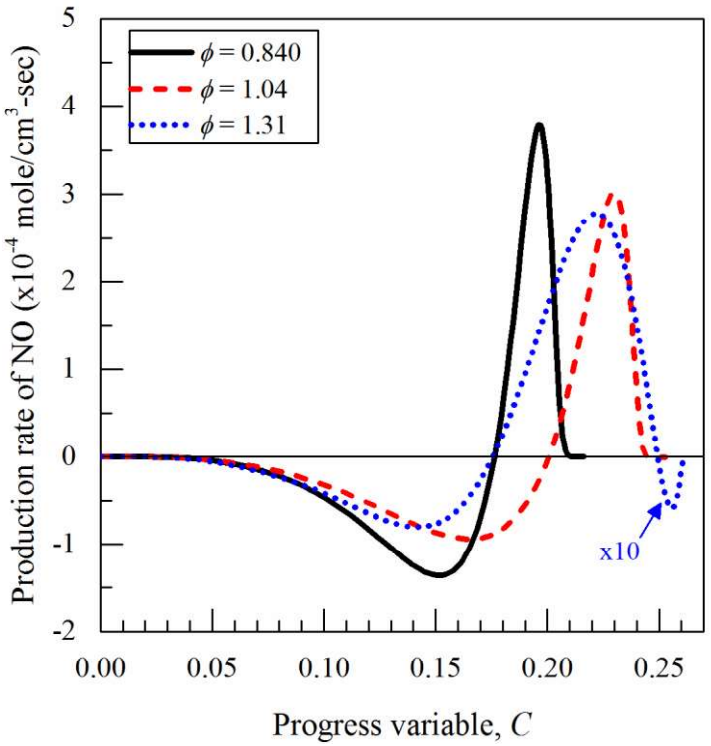

Fig. 8: Correlation between production rate of NO and progress variable, C, at ϕ = 0.840, 1.04 and 1.31for Δh = 0 (FGM).

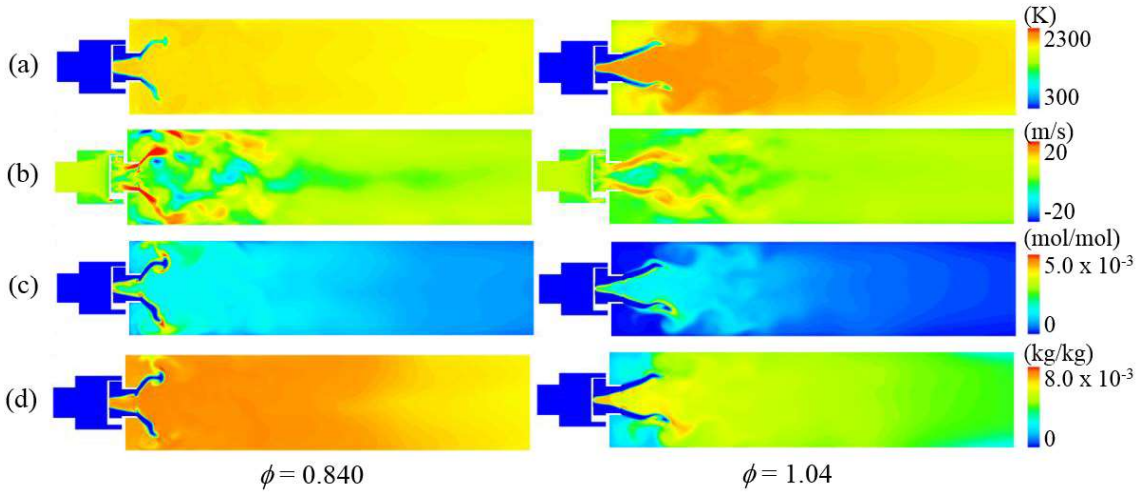

Fig. 9: Comparisons of instantaneous distributions of (a) temperature, (b) axial velocity, (c) OH mole fraction, and (d) NO mass fraction for LES/NA-FGM between the cases of ϕ = 0.840 and 1.04.

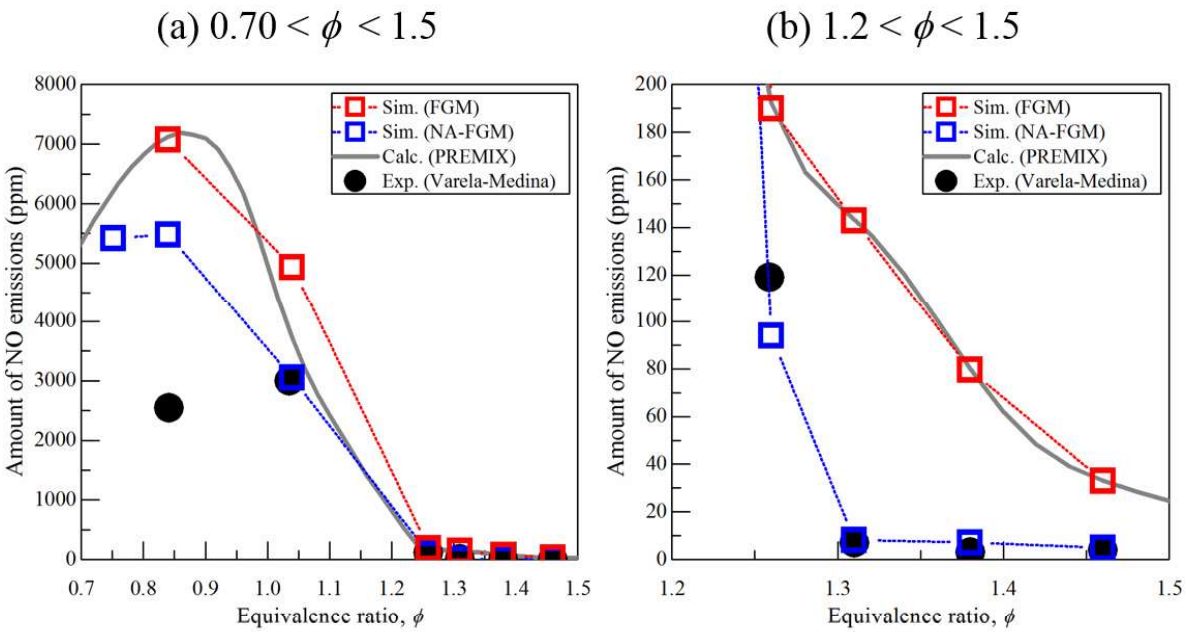

Fig. 10: Comparison of time-averaged amounts of NO emissions as a function of ϕ between LES/FGM and LES/NA-FGM, together with the results obtained by adiabatic one-dimensional premixed flame calculations (PREMIX) and experiments [15]. The display ranges are (a) $0.70 < \phi < 1.5$ and (b) $1.2 < \phi < 1.5$.

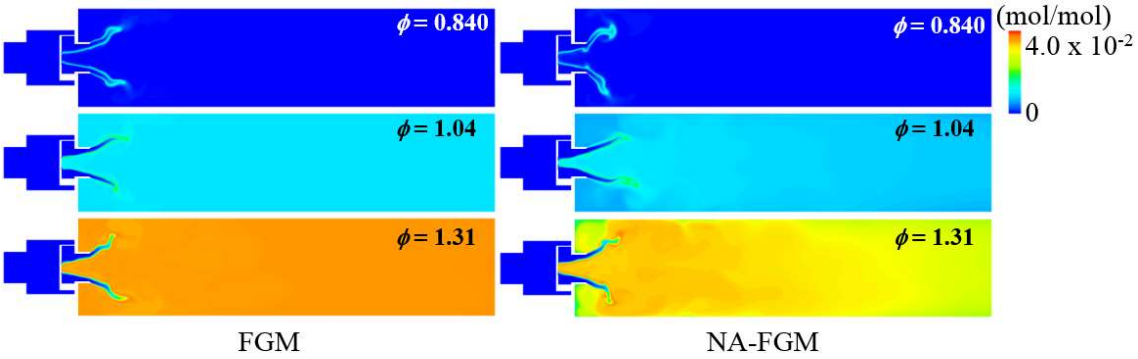

Fig. 11: Comparisons of instantaneous distributions of CO mole fraction at ϕ = 0.840, 1.04 and 1.31 between LES/FGM and LES/NA-FGM.

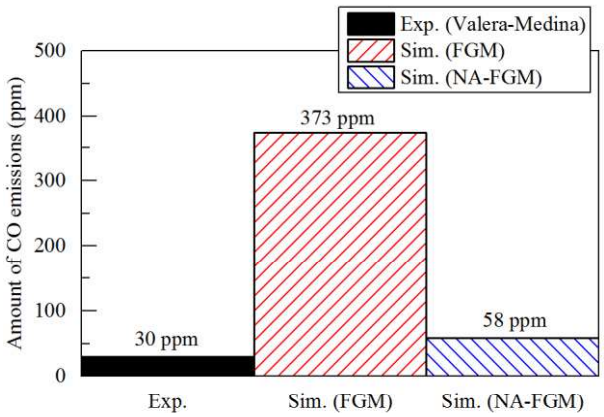

Fig. 12: Comparison of time-averaged amounts of CO emissions at ϕ = 0.840 between LES/FGM and LES/NA-FGM, together with experiments [15].

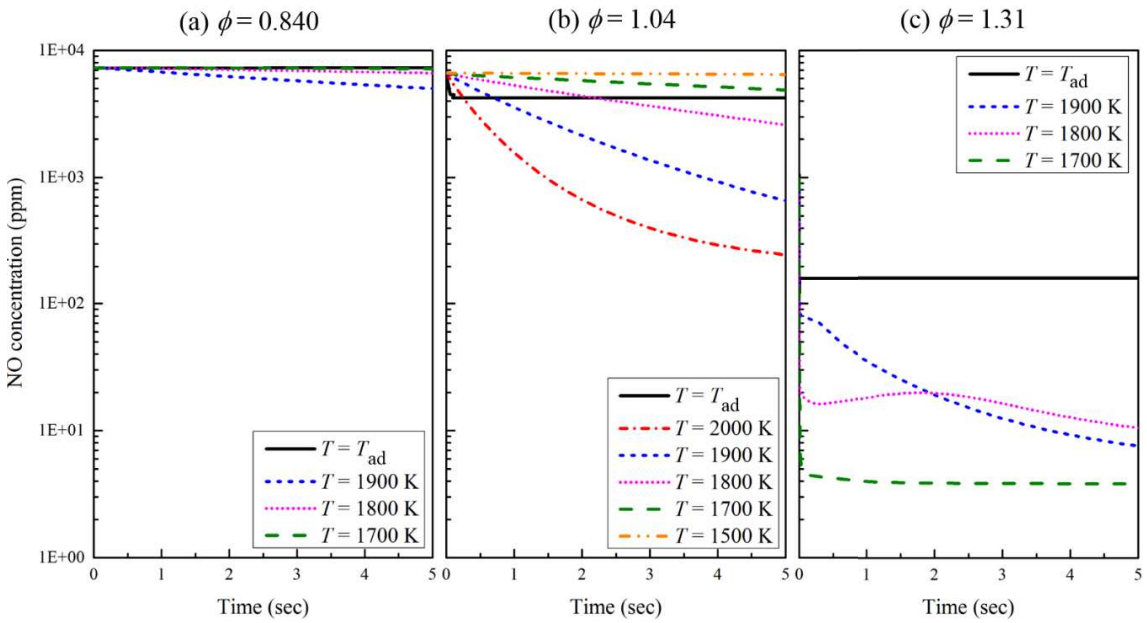

Fig. 13: Time series of NO concentrations at ϕ = 0.840, 1.04 and 1.31 for NH_3/CH_4/air combustion obtained by one-dimensional calculations in various temperature conditions.

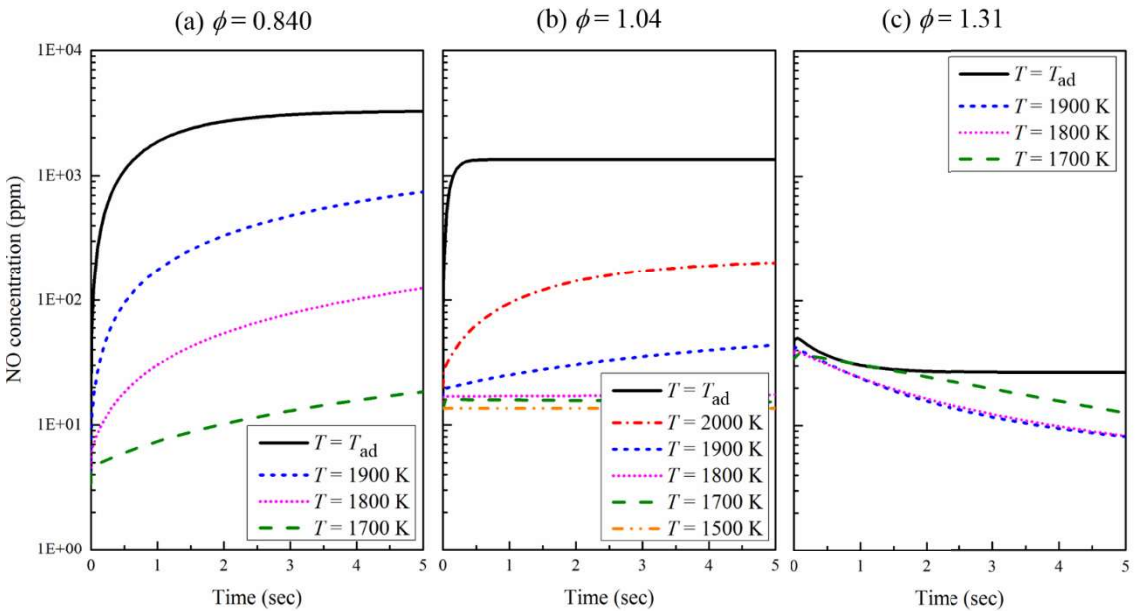

Fig. 14: Time series of NO concentrations at ϕ = 0.840, 1.04 and 1.31 for CH_4/air combustion obtained by one-dimensional calculations in various temperature conditions.

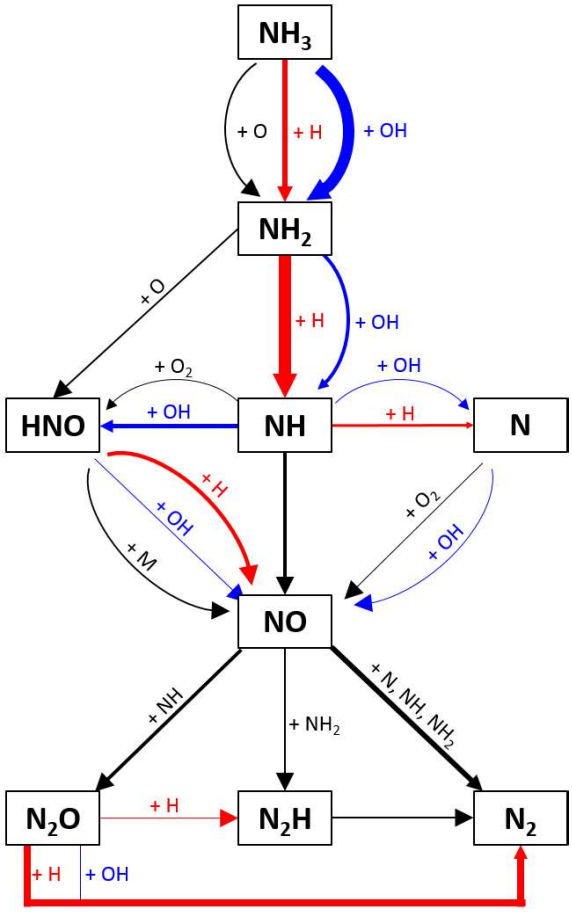

Fig. 15: Relevant reaction path related to NO concentration at ϕ = 1.31 for NH_3/CH_4/combustion at the time that its consumption rate is max by one-dimensional calculation in T = 1900 K.

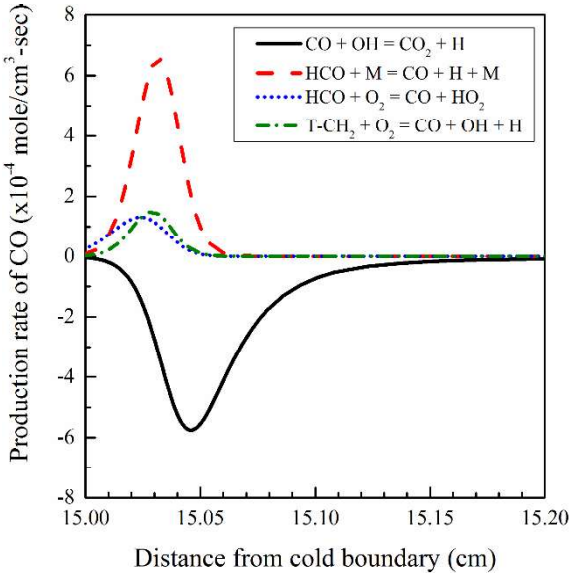

Fig. 16: Principal reactions of CO at ϕ = 0.840 for NH_3/CH_4/air obtained by one-dimensional calculation in an adiabatic condition.

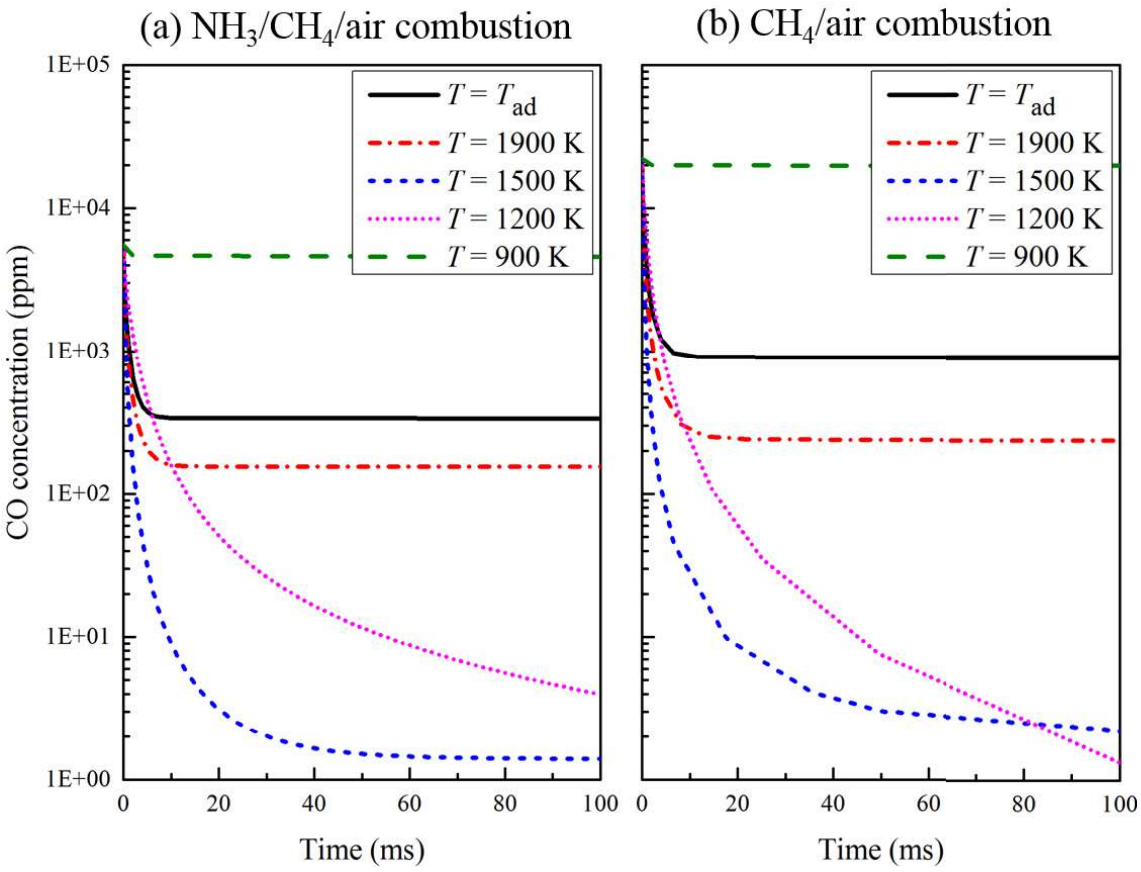

Fig. 17: Time series of CO concentrations at $\phi = 0.840$ for (a) NH_3/CH_4/air combustion and (b) CH_4/air combustion obtained by one-dimensional calculations in various temperature conditions.